Journal of Visualization, Vol. 8, No. 3 (2005)225-233

Improvement of Noise Filtering and Image Registration Methods for the Pressure Sensitive Paint Experiments

Fujimatsu, N.*[1], Tamura, Y.*[2] and Fujii, K.*[3]

*1 Department of Mechanical Engineering, Aoyama Gakuin University (Presently ISAS), 5-10-1 Kobuchi, Sagamihara, Kanagawa, 229-8558, Japan. E-mail: fujimatu@me.aoyama.ac.jp
*2 Department of Computational Science and Engineering, Toyo University, 2100 Kujirai, Kawagoe-shi, Saitama 350-8585, Japan. E-mail: tamtam@eng.toyo.ac.jp
*3 Institute of Space and Astronautical Science, Japan Aerospace Exploration Agency, 3-1-1 Yoshinodai, Sagamihara-shi, Kanagawa 229-8510, Japan. E-mail: fujii@flab.eng.isas.jaxa.jp

Received 13 August 2004
Revised 4 March 2005

Abstract : Image processing procedures for noise reduction and image registration in the Pressure Sensitive Paint (PSP) experiments are investigated. A several types of filter are examined for the removal of shot noise. An algorithm to detect a marker cell located on the model surface is proposed and an appropriate marker size is discussed. The digital processing based on the wavelet transform is effective to reduce the shot noise and to enhance the edge of the model. The algorithm to sharpen the edge of the model using wavelet transforms is developed. The results indicate that the methods developed in this study effectively remove the shot noise and correct the displacement of the model on the images taken during the wind-on.

Keywords : Flow Visualization, Post Image Processing, Pressure Sensitive Paint, Wavelet Transform.

1. Introduction

In recent years, research on surface pressure measurement using the PSP technique has increased in frequency (Bell et al., 2001; Mori et al., 2004). The PSP technique is becoming increasingly popular in wind tunnel testing due to the advantages of continuous pressure field measurement and reduced cost and time of experiments. Since PSP systems obtain pressure distributions from images captured by optical system devices, image processing is indispensable to obtain accurate pressure measurement and flow field images. Although the importance of image processing in PSP experiments has been reported in several studies, most of these discussions focus on the error induced in the measurement itself (Liu et al., 1999) and few reports have discussed the image processing technique. The major error sources in image processing are CCD camera noise called “shot noise” in the images, model displacement, pressure mapping and self-illumination by the model surfaces. Suitable filters to remove shot noise in PSP images have not been investigated. In 1993, Bell and McLachlan investigated image registration and discussed markers and the pressure mapping technique. They concluded that large model displacement requires the use of feature points of the model in addition to markers. However, the locations of feature points can not be determined because the model boundary in the image is obscure. For accurate, quantitative image registration, these points must be highlighted.

In the present study, noise filtering and image registration techniques are investigated for

accurate pressure measurements. The conventional noise filtering techniques are tested for the shot noise reduction, and two frequency filtering methods, the wavelet transformation and compact difference methods, are proposed as improved filtering methods. Affine transformation is commonly used for the image registration (Bell and McLachlan, 1993). However, a number of problems must be overcome to obtain accurate pressure distributions. One of these problems is the lack of a suitable algorithm to define the center of the marker location. Another problem is the difficulty in reading the feature points of the model from the image. In the present paper, a new algorithm for marker detection and enhancement of the feature points of models is proposed. Wind tunnel experiments using an Euler model (Erickson, 1991) are conducted to validate the proposed algorithm. The model used in the present experiment is identical to that used by the European Space Administration (ESA) for CFD Euler code validation. The surface pressure data obtained using the PSP is integrated, and the resultant lift coefficient is compared with force balance measurements.

2. Noise Filtering

Since images taken by CCD cameras include shot noise, the removal of the shot noise is necessary for accurate pressure measurement. Three types of traditional algebraic filter, the cell average, the median (Takagi and Shimoda, 1991), and selective local averaging (Tamura, 1985) are tested and compared. Figure 1 shows the flow field of the jet impingement over the plate.

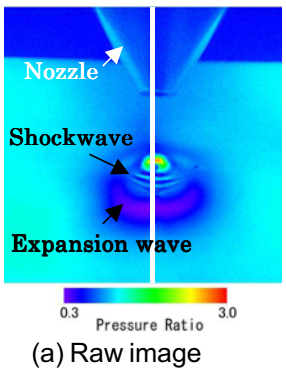

(a) Raw image

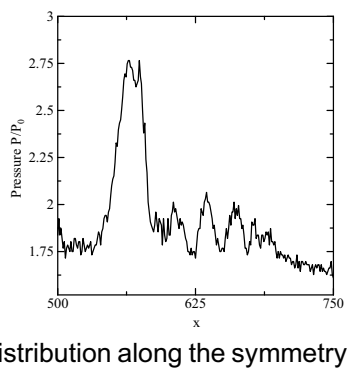

(b) Pressure distribution along the symmetry line of the plate

Fig. 1. Raw image before the shot noise removal.

Photographic images obtained in the jet impingement experiment (Nakai et al., 2001) are used as test images. The design Mach number is 2.0, and the nozzle pressure ratio at the nozzle exit is 3.0. The plate is positioned at an incline angle of 45 degrees. The non-dimensional distance from the nozzle exit to the plate surface (h/D) is set to 4.0. Twelve-bit color images are measured with a resolution of 1024 by 1024 pixels. The image obtained by averaging 50 raw images is assumed to be exact, and the error is evaluated by comparison to this image.

Figure 2 shows the pressure distributions along the symmetry line of the plate after each filter is operated ten times. Since the cell average filter is dissipative, shot noise is sufficiently removed. However, the shock wave has become obscure and the pressure peak is lost. The median filter removes the shot noise efficiently after four operations, as shown in Fig. 2, and does not smear the information even after repeated operations. Selective local averaging removes the shot noise efficiently after only two operations, and the filter effect becomes small after four operations. However, the result becomes obscure after ten operations. Both the median and selective local averaging create unphysical peaks during the operations. The arrows in Fig. 2 indicate these peaks that occur because the operations of taking the median cell or the cell of minimum dispersion is similar to advection. Therefore, these two filters should be applied carefully.

All three filtering methods are acceptable because the shot noise is clearly removed. However, these filters have some insufficiencies, as will later be shown quantitatively herein, and better filtering methods are required. Here, two new methods of frequency filtering are considered. The first is a spatial filtering method that was originally developed for the compact difference scheme in CFD simulations (Koutsavdis et al., 1999) and the other is a wavelet transform method.

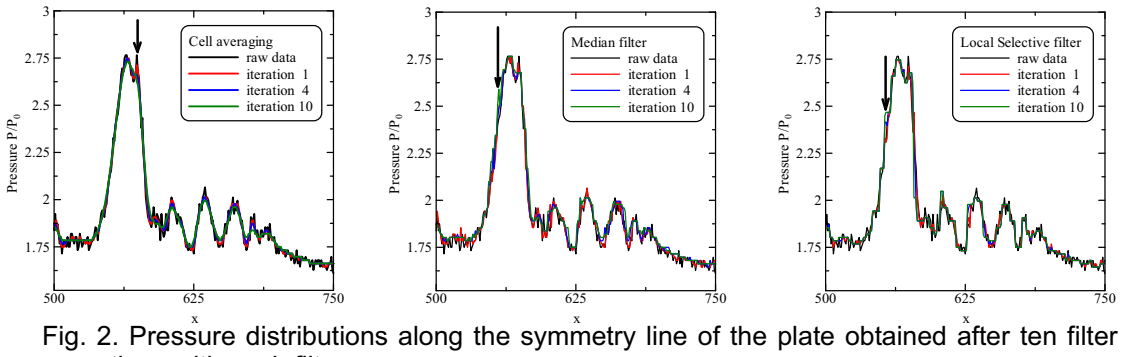

Fig. 2. Pressure distributions along the symmetry line of the plate obtained after ten filter operations with each filter.

Spatial filtering for the compact difference scheme is based on Fourier series expansion and was developed to eliminate undesirable high-frequency oscillations independent of the central differencing. This filter is referred to herein as a compact filter. The N-th order to an implicit filter is given by the following expression:

$$\alpha_f \hat{I}_{i+1} + \hat{I}_i + \alpha_f \hat{I}_{i-1} = \sum_{k=0}^{N/2} \frac{a_k}{2} (I_{i+k} + I_{i-k}) \tag{1}$$

where I and I' are original and filtered luminescence intensities, respectively. The coefficients of the right-hand side of the above expression depend on a single parameter family α_f. The coefficients of an eighth-order implicit filter are expressed as follows (Koutsavdis et al., 1999):

$$a_0 = \frac{93+70\alpha_f}{128}, \quad a_1 = \frac{7+18\alpha_f}{16}, \quad a_2 = \frac{-7+14\alpha_f}{32}, \quad a_3 = \frac{1-2\alpha_f}{16} \quad and \quad a_4 = \frac{-1+2\alpha_f}{128}$$

The strength of the filter can be controlled by changing the positive values of α_f. By reducing the value of α_f with its upper limit $\alpha_f = 0.5$, higher frequency wave components are removed. The value of $\hat{I}$ can be obtained by solving Eq. (1). Spatial filtering is applied to the x and y directions separately to eliminate any biasing effect (Koutsavdis et al., 1999).

Wavelet transform is used as an image processing tool in several applications (Sakakibara, 2001). In wavelet transform, an original image is decomposed into a set composed of a power spectrum for each wavelet component. The inverse wavelet transform is operated after high-frequency wavelet components are removed. Here, we assume that high-frequency wavelet components are due primarily to shot noise and low-frequency wavelet components correspond to the variation of physical variables. The basic process of noise removal using the wavelet transform is as follows: (1) Decompose the image using the wavelet transform to obtain the wavelet coefficients. (2) Decide the threshold value and neglect wavelet coefficients that are less than this threshold value. (3) Reconstruct the image using the inverse wavelet transform based on the remaining coefficients. The effect of the wavelet transform method can be controlled by the variation of the frequency level to be removed.

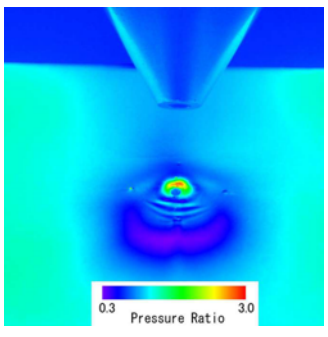

Fig. 3. Pressure image after noise filtering using the wavelet transform.

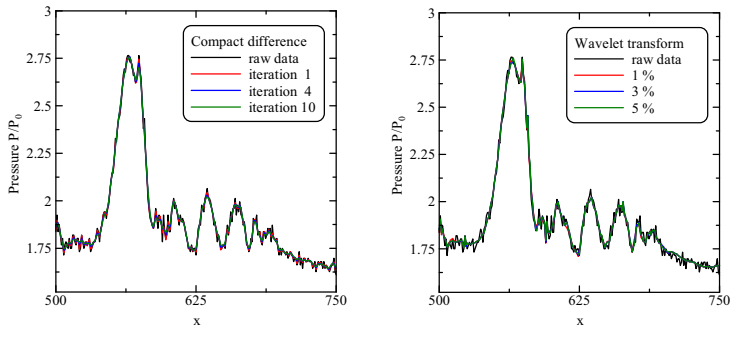

Fig. 4. Pressure distributions along the symmetry line of the plate obtained by compact difference $(\alpha_f = 0.4)$ and wavelet transform.

Figure 3 shows the reconstructed image maintaining 5% of the components of the wavelet coefficient. Figure 4 shows the filtered images obtained using the compact filter and the wavelet transform, respectively. As shown in Figs. 3 and 4, the filtered image obtained using the frequency filter successfully removes the shot noise. The compact filter and the wavelet transform method do not create unphysical peaks.

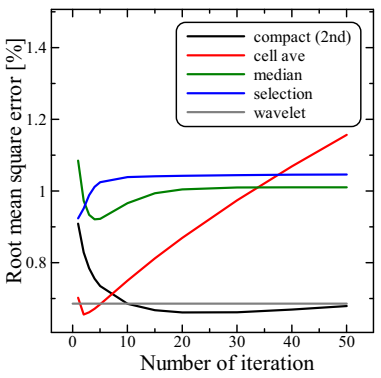

Fig. 5. Root mean square errors.

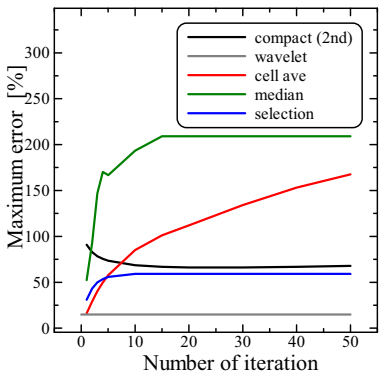

Fig. 6. Maximum errors.

In order to qualitatively discuss the effect of each filter, the error between exact images and filtered images is investigated. Figures 5 and 6 show the root mean square (RMS) error and the maximum error of the worst pixel, respectively. The result obtained by the wavelet transform method shows the error of the filtered image shown in Fig. 3. The cell average filter sufficiently removes the shot noise, and the RMS error decreases after a few operations. However, the maximum error increases as the shock wave smears out, and the RMS error also increases for the same reason after three operations. The RMS error of the median filter decreases due to the shot noise reduction up until four operations. However, the maximum error increases due to the unphysical peaks, and the RMS error also increases after four operations. Although selective local averaging effectively removes the shot noise, both the RMS error and the maximum error increase during the operations. The error caused by the appearance of unphysical peaks is greater than the effect of the noise reduction, as shown in Fig. 2. The RMS error of the compact filter decreases up until 25 operations to less than 0.7%. After 25 operations, the maximum error of the compact filter remains less than 70%. The RMS error and the maximum error obtained by the wavelet transform method are less than 0.7% and 20%, respectively. The wavelet transform method neither creates unphysical peaks nor smears the physical discontinuity.

Table 1 shows the computational time used to smooth the image by each filter. The rate is defined as the ratio of the computational time for each filtering method to the time required for the cell averaging. The computational times are measured for an 800-MHz Pentium III. The computational costs of the cell average, median and compact difference filters are less than those of the other filter. Selective local averaging is not effective with respect to computational time, and although the wavelet transform filter has a high computational cost for noise filtering, the noise is removed accurately. The total computational cost of wavelet transformation may be low compared the other filtering methods because wavelet transform filters improve the images through only one operation. Frequency filters such as the compact filter and the wavelet transform method developed herein are shown to have better compatibility than conventional filters.

Table 1. Computational cost for noise filtering per iteration.

	Rate	Time (sec)
Cell average	1.000	0.604
Median	1.227	0.741
Selective local averaging	6.566	3.966
Compact difference	0.909	0.549
Wavelet	8.142	4.918

3. Image Registration

3.1 Marker Detection

In wind-tunnel experiments, during the wind-on condition, the model moves slightly from its initial wind-off position. Therefore, the model displacement during the wind-on condition is another source of error for qualitative pressure measurement in PSP experiments. In most cases, image registration uses markers located on the model surface as reference points and affine transformation is used for image alignment. The marker points are checked visually to determine the pixel locations in the images. When image registration is performed as described above for a simple-capsule-like body, some pixel marker dislocation remains, as shown in Fig. 7. This error occurs because marker locations are checked visually. We therefore propose herein the following algorithm for marker detection: (1) Perform binary conversion of the image. (2) Manually input the position of one pixel located inside a marker. (3) Search for pixels having the same intensity level around the position of the input pixel. (4) Count the number of pixels having the same value. (5) Compute the total area. (5) Compute the equivalent circle having the same area of the marker. (6) Average the coordinates of the pixels having the same value and locate the center coordinate of the marker.

The appropriate marker size for correct marker detection is investigated to make this process feasible. A circle-shaped marker is positioned at (50.2 pixels, 50.4 pixels) in the x-y coordinate system. The size of the circle is then changed, and the marker location is determined using the algorithm described above.

Table 2 shows the obtained outputs for various marker radii. The algorithm detected the location and radius of the marker to the sub-pixel order only when the radius of the marker is greater than five pixels.

Table 2. Accuracy of maker detection.

Input of radius (pixels)	Output of the x coordinate	Output of the y coordinate	Output of the radius
1.0	Not detected	Not detected	Not detected
2.0	50.28571	50.50000	2.111004
3.0	50.21429	50.50000	2.985411
4.0	50.32653	50.42857	3.949327
5.0	50.21250	50.42500	5.046266
6.0	50.33333	50.43859	6.023897
7.0	50.27388	50.45860	7.069276

Image registration is conducted using the present marker detection algorithm. After detecting the marker visually or using the marker detection algorithm, affine transformation is performed to align the two images. Figure 8 shows the registration image obtained using this algorithm. The model displacement at the base region is modified, and the image registration is performed successfully, as shown in Fig. 7, although model displacement remains at the body boundary.

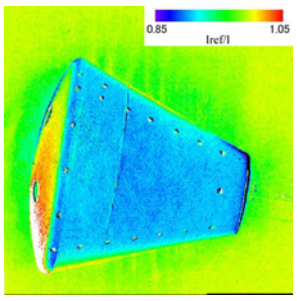

Fig. 7. Corrected registration image obtained using the visually detected marker location.

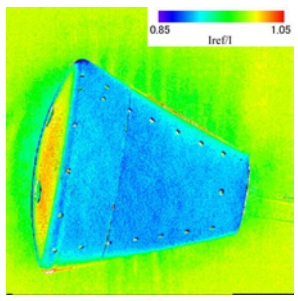

Fig. 8. Corrected registration image obtained using the marker detection algorithm.

3.2 Edge Enhancement Method

Even a small displacement induces a serious error when calculating the aerodynamic forces using PSP measurement. Therefore, in order to further reduce the displacement error, the corner of the base region and the junction of the model are used as reference points. However, the model boundary is obscure, as shown in Fig. 9, and these points must be highlighted using the raw images. Laplacian and gradient filters were tested and compared. Figure 10 shows the luminescence intensity

distribution along the vertical line in Fig. 9. Conventional methods are usually sensitive to noise components. The images obtained by these methods include strong noise components, as shown in Fig 10. The location of the edge can not be determined using Fig. 10. Although edge extraction from the image after the removal of the noise has been considered, the details of the luminescence intensity may be lost.

The location of the edge in the image roughly corresponds to the location of the high-frequency components of the image. In image processing software, edge enhanced algorithm is conducted by amplifying these components. However, the above-described method can not be simply used to correctly detect the location of the edge because this location is created by the superposition of the wave components of each frequency.

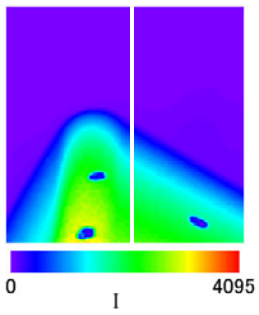

Fig. 9. Raw image with obscure edge.

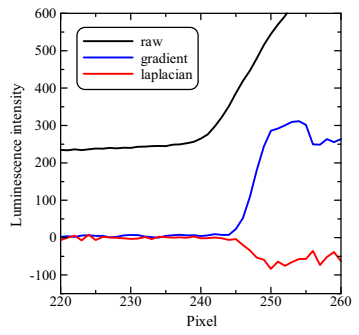

Fig. 10. Luminescence intensity distributions obtained by the conventional methods.

We therefore propose a new algorithm for edge enhancement. The luminescence intensity measured in a PSP experiment can be written as the following equation:

$$I(x,y) = G \otimes I'(x,y) + n(x,y) \tag{2}$$

where I' is the ideal luminescence intensity with sharp edges, n is the shot noise component, G is the noise source that obscures the model boundary, and $\otimes$ indicates the convolution of function G and image I'. The image I' with sharp edges can be obtained when G^{-1} is operated on Eq. (2). The inverse transform of Eq. (2) is as follows:

$$I'(x,y) = G^{-1} \otimes (I(x,y) - n(x,y)). \tag{3}$$

The raw image I is decomposed using a multi-resolution analysis, which is conceptually similar to the Mallat wavelet (Mallat, 1989). The Mallat wavelet can be interpreted as the decomposition of the image by a series of independent-frequency components. A method similar to the Mallat wavelet is the Laplacian pyramid (Burt and Anderson, 1983). In the Laplacian pyramid representation, the reference image is a Gaussian smoothed image and the detail images can be obtained as by comparison to the Gaussian filter, which is very similar to the LOG filter (Wilson and Bergen, 1979).

Based on the above-described scheme, the edge enhancement algorithm is developed. The Mexican hat function, which is similar to the LOG filter, is used as the wavelet basis. The two-dimensional Gaussian function and the LOG function in polar-coordinate form are as follows:

$$G_{A_j}(r) = \frac{1}{2\pi\sqrt{A_j}} \exp\left(-\frac{r^2}{A_j}\right), \quad \psi_A(r) = \frac{1}{2\pi A_j}\left(1-\frac{r^2}{A_j}\right)\exp\left(-\frac{r^2}{A_j}\right) \quad and \quad r = \sqrt{x^2+y^2} \tag{4}$$

where A_j is the dispersion value, G_{A_j} is the Gaussian function with A_j, and ψ_{A_j} is the Laplacian of G_A with A_j. The raw image is filtered by the Gaussian function to yield the reference image. Then, at each frequency level *j*, the residual image is decomposed using the wavelet transform. The original image I is decomposed as Eq. (5):

$$I = G_{A_0} \otimes I + \sum_{j=1}^{J}\sum_{k} WI_{j,k}\psi_{A_j,j,k} + I_{J+1} \tag{5}$$

The highest frequency components, I_{J+1}, are removed because they are considered to

represent the shot noise components *n*. $WI_{j,k}$ corresponds to the discrete wavelet transform and is defined as

$$WI_{j,k} = \sum_i I(x^i)\psi_{A_j,j,k}(x^i)\cdot \tag{6}$$

When Eq. (5) is substituted to Eq. (3), the inversion process for the edge enhancement is obtained as Eq. (7):

$$I' = G_{-B} \otimes \left(G_{A_0} \otimes I + \sum_{j=1}^{J} \sum_k WI_{j,k}\psi_{A_j,j,k} \right) = G_{A_0-B} \otimes I + \sum_{j=1}^{J} \psi_{A_j-B,j,k} \otimes WI_{j,k} \tag{7}$$

The convolutions between $\psi_{j,k}$ and $WI_{j,k}$ represent the wavelet components. In Eq. (7), G_{-B} corresponds to G^{-1} in Eq. (3). The original image is reconstructed using Eq. (8). The strength of the edge enhancement is controlled by the variation of B . Here, we set $A_0 = 1.5$, $A_1 = 2.3$, $A_{j+1} = 0.8\ A_j (j > 1)$, $B = 0.7$ and $J = 4$. Figure 11 shows the image with the highlighted model boundary. The enhanced image clearly captures the base region. Figure 12 shows the comparison of the luminescence intensity distribution of the raw image and the modified image obtained by the edge enhancement. A sharp image is obtained using Eq. (7) with few induced oscillations. Using this feature point detection algorithm, another image registration is tried. Here, we use the corner of the base region as reference points. Figure 13 shows the divided image obtained by the marker detection and the edge enhanced algorithms. The result in Fig. 13 clearly shows that the model displacement is removed.

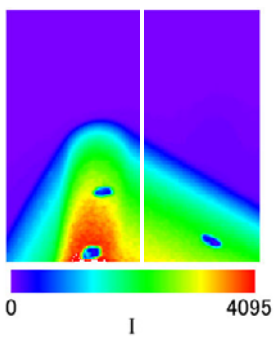

Fig. 11. Highlighted edge of the modified image.

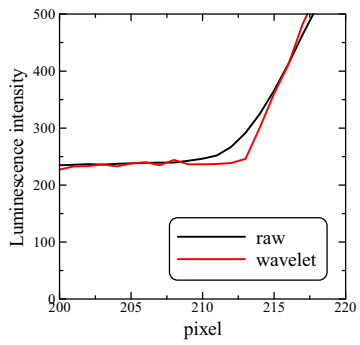

Fig. 12. Highlighted intensity obtained using wavelet transform.

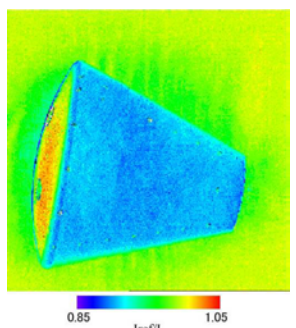

Fig. 13. Corrected image obtained feature points and the marker detection algorithm.

4. Practical Application

In order to valid these techniques, we conducted a wind tunnel experiment using an Euler model. The experiment is carried out using the transonic wind tunnel at the ISAS/JAXA in Japan. The Euler model used in the experiment has a sweep angle of 65 degrees, a taper ratio of 0.15, and a model chord length of 150 mm. PSP and TSP are partially painted on each side of the model surface. The temperature dependency of the PSP is removed using the TSP. A detailed description of the method to remove the temperature dependency is presented by Nakai et al (2003). The PSP data is compared with that obtained in a previous experiment at NASA (Erickson, 1991).

Figures 14(a) and (b) are image before and after image registration, respectively. The black circles shown in the figures indicate the locations improved by the image registration. The model displacement at the corner of the wing tip and the apex of the wing can be removed using the present marker detection and edge enhancement algorithms. Figure 15 shows the raw pressure data without image alignment or noise filtering and the filtered pressure data obtained using the PSP. The wavelet transform is used for noise filtering. The black line shows the pressure tap data (Erickson, 1991), which match the PSP results. Figure 16 shows the pressure data mapped onto the coordinates of the Euler model using Direct Linear Transform (DLT) (Bell and McLachlan, 1993). Once the pressure data has been transposed onto the surface definition grid, the aerodynamic data can be easily computed as the integral of the pressure distribution over the model surface. Figure 17 shows

the lift-slope curve obtained using the PSP, where C_L and α are the total lift coefficient and the angle of attack, respectively. The inverted triangle symbol shows the data for the balance measurement. The ○ and × symbols indicate the C_L values obtained with and without our image processing, respectively. Although the PSP data only includes the C_L values obtained by the pressure integration, while the contribution by skin friction is neglected, the qualitative characteristics can be successfully captured using the PSP. The flow is highly unsteady at high angles of attack due to vortex bursting, and the lift characteristics may vary by experiment. A 3% measurement error exists between the results obtained with and without the present algorithm. These results show that the methods presented herein are effective for accurate quantitative PSP measurement.

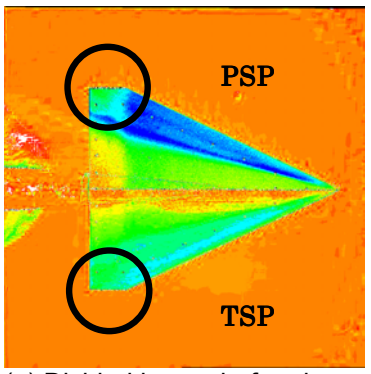

(a) Divided image before image registration.

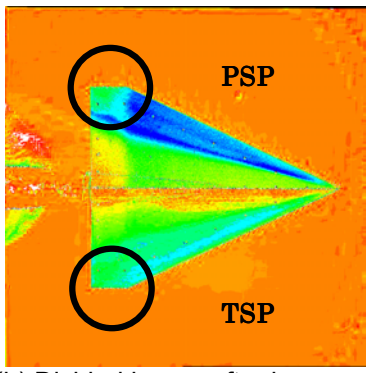

(b) Divided image after image registration.

Fig. 14. Corrected image obtained using the marker detection algorithm $(M_\infty = 0.9, \alpha = 16°)$.

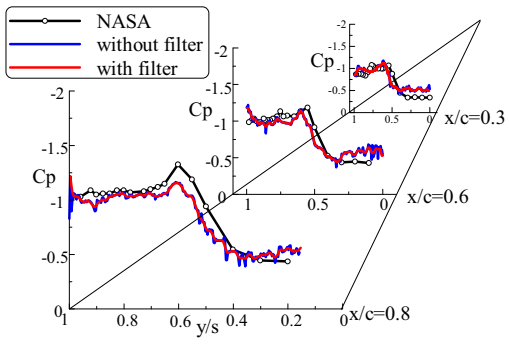

Fig. 15. Comparison of PSP data with Pressure tap data for wing upper-surface pressure distributions $(M_\infty = 0.9, \alpha = 16°)$.

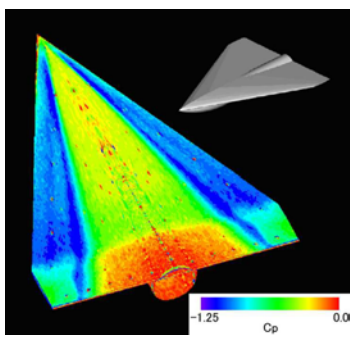

Fig. 16. Surface pressure distribution mapped on to the wing surface $(M_\infty = 0.9, \alpha = 16°)$.

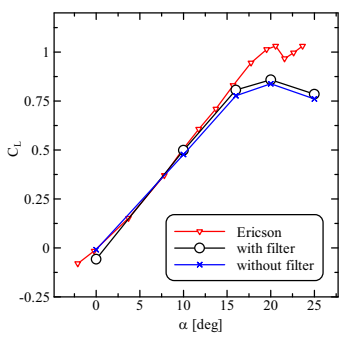

Fig. 17. $C_L - \alpha$ characteristics at $M_\infty = 0.9$.

5. Conclusions

Filtering techniques to remove shot noise and an image registration technique for PSP experiments were investigated. New frequency filters, such as the compact filter and wavelet transform, are most suitable for shot noise reduction. Although conventional algebraic filters can remove shot noise, these filters have a number of shortcomings. For image registration, two types of algorithms, for marker detection and edge enhancement, are proposed. The marker size should be more than five pixels in radius to capture the sub-pixel location. The displacement of the model during the wind-on condition can be accounted for using the newly developed algorithm together with markers and feature points. Computational costs can be effectively reduced because edge enhancement and removal of shot noise are achieved simultaneously using the wavelet transform. The aerodynamic force (C_L) was accurately computed based on the surface pressure distribution obtained by the PSP technique.

Acknowledgement

This research is partially supported by the "Molecular Sensors for Aero-Thermodynamic research (MOSAIC)" program, the special coordination founds of the Ministry of Education, Science, Sports and Culture. The authors would like to thank Dr. Keisuke Asai, currently Professor at Tohoku University, the leader of the MOSAIC program, for the stimulating discussions on the present research.

References

Bell, J. H. and McLachlan, B. G., Image Registration for Luminescence Paint Sensors, AIAA Paper 93-0178, 31st Aerospace Sciences Meeting & Exhibit, (1993).
Egami, Y., Iijima, Y., Amao, Y., Asai, K., Fuji, A., Teduka, N. and Kameda, M., Quantitative Visualization of the Leading-edge Vortices on a Delta Wing by Using Pressure-sensitive Paint, J. of Visualization, 4-2 (2004), 139-150.
Burt, P. J. and Andelson, E. H., The Laplacian pyramid as a compact image code, IEEE Trans. Commun., 31-4 (1983), 532-540.
Erickson, G. E., Wind Tunnel Investigation of the Interaction and Breakdown Characteristics of Slender-Wing Vortices at Subsonic, Transonic and Supersonic Speeds, NASA-TP3116, (1991).
Koutsavdis, E. K., Blaisdell, G. A., Lyrintzis, A. S., A Numerical Investigation of Two Dimensional Jets using Spatial Filtering, 5th AIAA/CEAS Aeroacoustics Conference, AIAA-Paper 99-3706, 37th Aerospace Sciences Meeting & Exhibit, (1999).
Liu, T., Guille, M. and Sullivan, J. P., Accuracy of Pressure Sensitive Paint, AIAA Paper 99-3785, 37th Aerospace Sciences Meeting & Exhibit, (1999).
Mallat, S. G., A theory for multiresolution signal decomposition: The wavelet representation, IEEE Trans. Pattern Anal. & Mach. Intell., 11-7 (1989), 672-693.
Mori, H., Niimi, T., Yoshida, M., Kondo, M., and Oshima, Y., Application of PSP to Low Density Gas Flows, J. of Visualization, 7-1 (2004), 55-62.
Nakai, Y., Fujimatsu, N. and Fujii, K., Flow Classification of the Under-Expanded Super Sonic Jet Impinging on a Flat Plate, 21st AIAA Applied Aerodynamics Conference, AIAA 2003-3467 (2003).
Sakakibara, S., Introduction to Wavelet Transform, J. of the visualization society of Japan, 21-82 (2001), 1-6 (in Japanese).
Takagi, M. and Shimoda, H., Handbook for Image Processing, (1991), Tokyo University Press (in Japanese).
Tamura, H., Introduction to Image processing, (1985), Ohmusha (in Japanese).
Wilson, H. R. and Bergen, J. R., A four mechanism models for spatial vision, Vision Res., 19-1 (1979), 19-32.

Author Profile

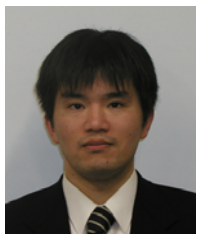

Nobuyoshi Fujimatsu: He received his M.Sc.(Eng) in Aerospace Engineering in 1998 from University of Tokyo. He also received his Ph.D. in Aerospace Engineering in 2001 from University of Tokyo. He worked for Research Division for Space Transportation, the Institute of Space and Astronautical Science as a research associate in 2001. He works in Department of Mechanical Engineering, Aoyama Gakuin University as a research associate since 2003. His research interests are computational fluid dynamics, flow visualization, image processing and turbulence flow.

Yoshiaki Tamura: He received his master degree of engineering in the Department of Aeronautics and Astronautics, University of Tokyo in 1986. He worked for Fujitsu Ltd. for three years as a systems engineer before he started his research carrier at the Institute of Space and Astronautical Science (ISAS). After spending seven and a half years at the ISAS as a research associate, he became an associate professor at Intelligent Modeling Laboratory, University of Tokyo in 1996. From 2001, he is an associate professor of the Department of Computational Science and Engineering, Toyo University. His major research field is computational fluid dynamics, especially numerical algorithms, cavitating flow simulations and visualization using computer graphics and virtual reality.

Kozo Fujii: He received his Ph.D. in the Department of Aeronautics, University of Tokyo in 1980. After spending several years at NASA Ames Research Center as a (senior) NRC research associate and (senior) research scientist at National Aerospace Laboratory in Japan, he became an associate professor at the Institute of Space and Astronautical Science in 1988. After the reorganization of Japanese aerospace institutes on 2003, he is currently a professor of the department of space transportation engineering at the Institute of Space and Astronautical Science, Japan Aerospace Exploration Agency. His research area spreads all the aspects of fluid dynamics including flow visualizations.